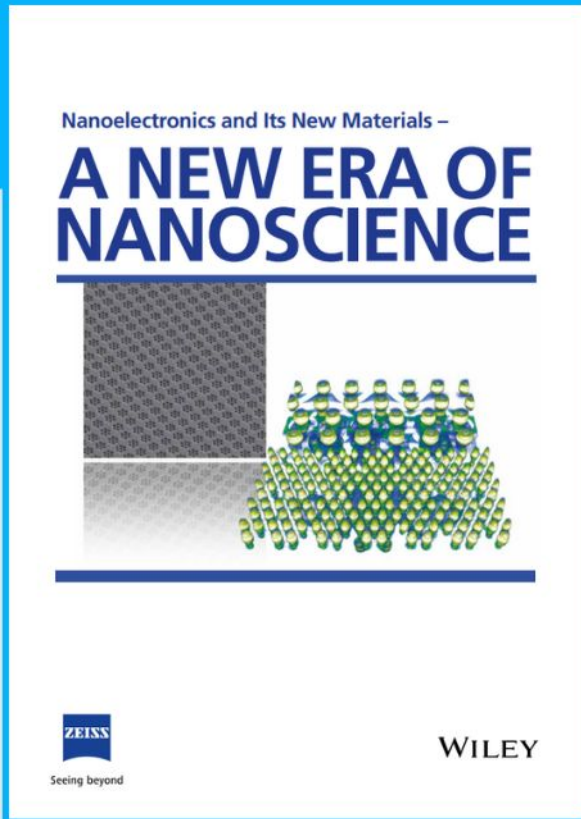




# Nanoelectronics and Its New Materials – A NEW ERA OF NANOSCIENCE



**Discover the recent advances in electronics research and fundamental nanoscience.**

Nanotechnology has become the driving force behind breakthroughs in engineering, materials science, physics, chemistry, and biological sciences. In this compendium, we delve into a wide range of novel applications that highlight recent advances in electronics research and fundamental nanoscience. From surface analysis and defect detection to tailored optical functionality and transparent nanowire electrodes, this eBook covers key topics that will revolutionize the future of electronics.

To get your hands on this valuable resource and unleash the power of nanotechnology, simply download the eBook now. Stay ahead of the curve and embrace the future of electronics with nanoscience as your guide.



Seeing beyond

**WILEY**

# 3D Printing of Multifunctional Conductive Polymer Composite Hydrogels

Ji Liu,\* James Garcia, Liam M. Leahy, Rijian Song, Daragh Mullarkey, Ban Fei, Adrian Dervan, Igor V. Shvets, Plamen Stamenov, Wenxin Wang, Fergal J. O'Brien, Jonathan N. Coleman, and Valeria Nicolosi\*

Functional conductive hydrogels are widely used in various application scenarios, such as artificial skin, cell scaffolds, and implantable bioelectronics. However, their novel designs and technological innovations are severely hampered by traditional manufacturing approaches. Direct ink writing (DIW) is considered a viable industrial-production 3D-printing technology for the custom production of hydrogels according to the intended applications. Unfortunately, creating functional conductive hydrogels by DIW has long been plagued by complicated ink formulation and printing processes. In this study, a highly 3D printable poly(3,4-ethylenedioxythiophene):polystyrene sulfonate (PEDOT:PSS)-based ink made from fully commercially accessible raw materials is demonstrated. It is shown that complex structures can be directly printed with this ink and then precisely converted into high-performance hydrogels via a post-printing freeze–thawing treatment. The 3D-printed hydrogel exhibits high electrical conductivity of  $\approx 2000 \text{ S m}^{-1}$ , outstanding elasticity, high stability and durability in water, electromagnetic interference shielding, and sensing capabilities. Moreover, the hydrogel is biocompatible, showing great potential for implantable and tissue engineering applications. With significant advantages, the fabrication strategy is expected to open up a new route to create multifunctional hydrogels with custom features, and can bring new opportunities to broaden the applications of hydrogel materials.

## 1. Introduction

Hydrogels are polymer networks containing a large amount of water, which have attracted significant attention across various engineering disciplines due to their biocompatibility and broadly tunable physicochemical properties.<sup>[1–5]</sup> Despite remarkable advances, the current manufacturing and processing of functional hydrogels rely mainly on conventional techniques (e.g., casting, modeling, and subtractive manufacturing), which have severely hampered the development of technological innovations using hydrogel materials.<sup>[6]</sup> Therefore, it is desired to develop custom fabrication of hydrogels, which means that the hydrogels should be fabricated in a controllable way to possess specific composition, geometry, structure, and performances according to the intended application scenarios. Different from conventional techniques, additive manufacturing, also known as 3D printing, has been considered a viable industrial technology

J. Liu, J. Garcia, D. Mullarkey, B. Fei, I. V. Shvets, P. Stamenov, J. N. Coleman, V. Nicolosi  
Centre for Research on Adaptive Nanostructures and Nanodevices (CRANN) and Advanced Materials Bio-Engineering Research Centre (AMBER)  
Trinity College Dublin  
DublinIreland  
E-mail: ji.liu@tce.ie; nicolov@tcd.ie


J. Liu, V. Nicolosi  
School of Chemistry  
Trinity College Dublin  
DublinIreland

J. Garcia, D. Mullarkey, I. V. Shvets, P. Stamenov, J. N. Coleman  
School of Physics  
Trinity College Dublin  
DublinIreland

L. M. Leahy, A. Dervan, F. J. O'Brien  
Tissue Engineering Research Group  
Department of Anatomy & Regenerative Medicine  
Royal College of Surgeons in Ireland (RCSI)  
DublinIreland

R. Song, W. Wang  
Charles Institute of Dermatology  
School of Medicine  
University College Dublin  
DublinIreland

F. J. O'Brien  
Trinity Centre for Biomedical Engineering (TCBE)  
Trinity College Dublin  
DublinIreland

 The ORCID identification number(s) for the author(s) of this article can be found under <https://doi.org/10.1002/adfm.202214196>

© 2023 The Authors. Advanced Functional Materials published by Wiley-VCH GmbH. This is an open access article under the terms of the Creative Commons Attribution License, which permits use, distribution and reproduction in any medium, provided the original work is properly cited.

DOI: 10.1002/adfm.202214196

for the cost-effective, precise, and reproducible production of materials with features tailored to real needs of users.<sup>[6,7]</sup> Hitherto, various 3D-printing techniques, such as digital light process (DLP),<sup>[8,9]</sup> stereolithography,<sup>[10]</sup> two-photon polymerization (TPP) microfabrication,<sup>[11]</sup> and direct ink writing (DIW)<sup>[12,13]</sup> have been developed for the custom fabrication of hydrogel devices. Among them, DIW is most suitable for creating functional hydrogels, as it does not require nonfunctional components (e.g., photosensitized monomers for DLP and TPP) that may affect the functionality of the printed devices.<sup>[14]</sup> However, to enable successful 3D printing of functional hydrogels by DIW, precursor inks should be modified to possess suitable rheological properties (e.g., high viscosity, proper moduli, and shear-thinning behavior). Besides, efficient post-printing treatments are generally required for converting the printed soft ink filaments into integrated hydrogels while not affecting the shape fidelity of the printed structure. These requirements are a major obstacle to realizing the full potential of DIW for functional hydrogel manufacturing.

Conducting polymers, such as poly(3,4-ethylenedioxythiophene):polystyrene sulfonate (PEDOT:PSS), exhibit unique advantages because of their combination of intrinsic electrical conductivity and other advantageous properties derived from the polymeric nature (e.g., good mechanical properties, stability, and biocompatibility), demonstrating great potential for various applications including energy storage,<sup>[15,16]</sup> flexible electronics,<sup>[17,18]</sup> sensing,<sup>[19]</sup> and electromagnetic interference (EMI) shielding.<sup>[20,21]</sup> In particular, PEDOT:PSS has excellent hydrophilicity, and is easily soluble in aqueous media to form viscous inks that can be directly used for DIW.<sup>[13]</sup> When the PEDOT:PSS inks are properly designed to have the right rheological properties, they can exhibit favorable 3D printability.<sup>[13]</sup> However, the printed pristine PEDOT:PSS hydrogels still suffer from inferior conductive and mechanical properties. The existence of hydrophilic and insulative PSS component guarantees easy solution processability of PEDOT:PSS but inevitably leads to low conductivity of the printed devices.<sup>[13,15]</sup> Some efficient post-treatments (e.g., thermal annealing) can remove the PSS phase to restore the high conductivity and improve the mechanical properties.<sup>[4,15]</sup> However, the shape and structure of the printed devices are severely affected due to the fast compositional and morphological changes, resulting in low printing fidelity.<sup>[4,20,22]</sup> To date, a general 3D-printing strategy that allows the precise and scalable production of high-performance conductive PEDOT:PSS-based hydrogels by DIW is still highly required. Furthermore, such a strategy must involve fully commercially accessible raw materials and simple fabrication, which are necessary for the progress from the laboratory to commercial applications.

Here, we demonstrate that the goals aforementioned can be easily achieved by developing 3D printable PEDOT:PSS-based inks containing carbon nanotubes (CNTs) as both ink modifier and functional additive. By adding freeze-dried PEDOT:PSS (Clevios PH1000, Heraeus) into commercially available aqueous CNTs dispersions (Tuball, OCSiAl), we show that highly printable inks suitable for DIW can be simply formulated at low PEDOT:PSS concentrations (>20 mg mL<sup>-1</sup> PEDOT:PSS), without using any organic solvent. Through a post-printing freeze-thawing treatment, the printed objects can be directly and pre-

cisely converted into high-performance functional hydrogels, in which the CNTs arrange themselves into the polymer matrix to form a unique reinforced conductive network, ensuring outstanding electrical conductivity and mechanical properties. The resulting composite hydrogel has a very high conductivity of  $\approx 2000 \text{ S m}^{-1}$ , good stability and durability in water, and excellent elasticity with a recoverable strain of 80% and fatigue resistance, which further enable outstanding EMI shielding and pressure sensing capabilities. Moreover, the 3D-printed composite hydrogel is highly biocompatible and can provide a neurotrophic environment to support sensitive neuronal cell growth, demonstrating strong potential for implantable and tissue engineering applications.

## 2. Results and Discussion

**Figure 1a** illustrates the preparation process of the 3D printable composite inks from the freeze-dried PEDOT:PSS and CNTs dispersions by wet milling. The freeze-dried PEDOT:PSS is hydrophilic and can be rapidly infiltrated by the aqueous CNTs dispersions (Figure S1, Supporting Information). After mixing and grinding in the mortar, paste-like inks were obtained. Since all the raw materials are commercially available, the ink preparation strategy is readily scalable to enable large-scale production. The prepared inks were stored at a low temperature ( $\approx 4 \text{ }^\circ\text{C}$ ) before use and exhibited a long shelf life (more than 6 months) (Figure S2, Supporting Information). In addition, the aqueous ink does not contain any organic solvents and harmful additives, which greatly simplifies the ink preparation process and would reduce the issues linked to the ink storage, transportation, and printing processes. The printability of the inks was then investigated by studying their rheology. Figure 1b shows that all the inks have a distinct shear-thinning behavior, which is necessary for smooth extrusion during DIW. Note that the apparent viscosity of the composite ink is orders-of-magnitude higher than that for pure polymer ink at the same PEDOT:PSS concentration. This desired enhancement of viscosity and the significant shear-thinning behavior are likely to be due to the reversible hydrogen bonding and physical interactions (e.g., chain entanglement) among the components with high aspect ratios.<sup>[23]</sup> Correspondingly, using the CNTs dispersion to dissolve the PEDOT:PSS also brings a remarkable increase in the moduli and yield stress of the resulting composite inks, which ensures that the deposited ink filaments can maintain their stable shape without collapsing during the printing process (Figure 1c,d). To visualize this, both the pure polymer ink and composite ink were deposited on a plastic substrate by extrusion from a common syringe (Figure 1e). It was observed that the filaments of the pure polymer inks extruded from a syringe rapidly merged and spread on the substrate (Figure 1e-I,II), whereas the composite inks showed a good shape fidelity (Figure 1e-III-V). These results confirmed the satisfactory 3D printability of the composite ink even at low PEDOT:PSS concentrations. Since the ink rheology can be easily tuned by changing the PEDOT:PSS concentration, further solvent evaporation steps commonly used for concentrating the ink can be avoided, greatly simplifying the ink formulation.<sup>[23]</sup>

With the prepared highly printable composite ink (40 mg mL<sup>-1</sup> PEDOT:PSS, 2 mg mL<sup>-1</sup> CNTs), freestanding 3D composite structures with complex shapes can be directly and accurately



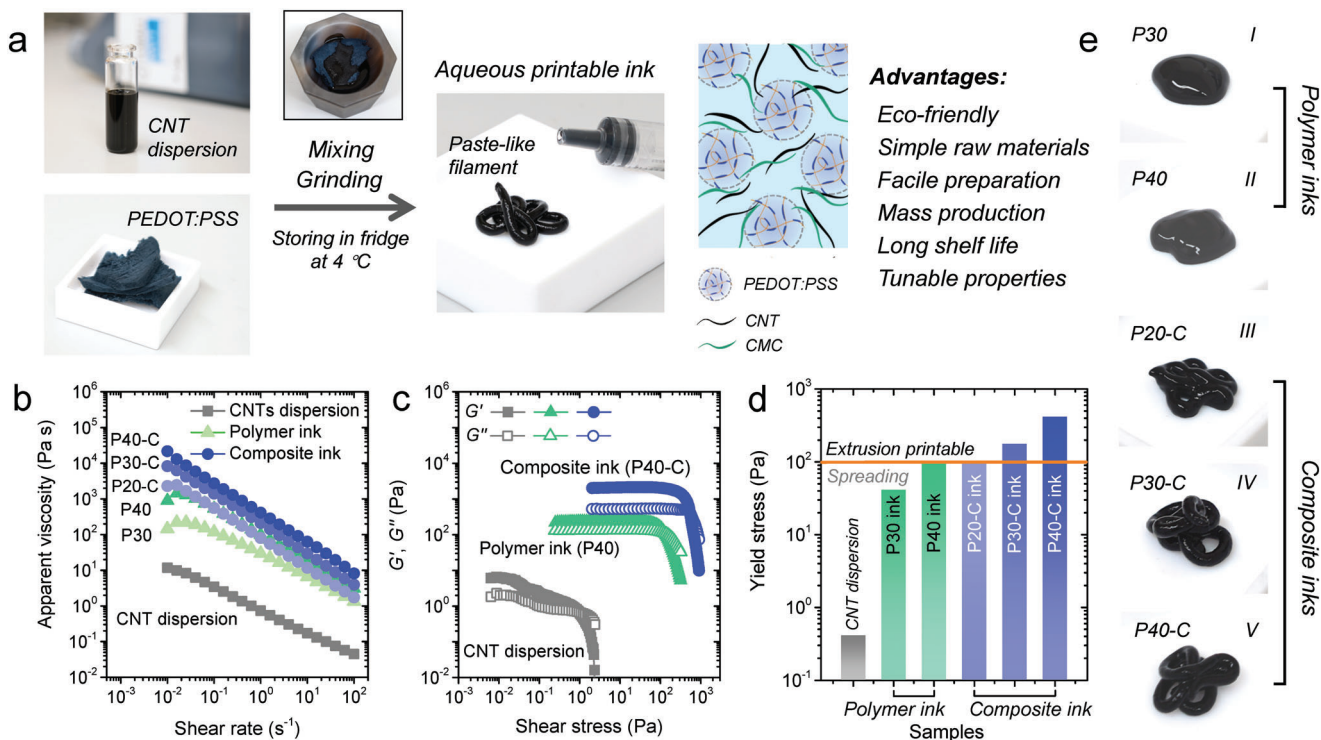


**Figure 1.** Design of 3D printable composite inks for additive manufacturing. a) Preparation process of the composite inks for DIW. b–d) Rheological properties (viscosity, moduli, yield stress) of different inks (the polymer and composite inks were termed as  $P_x$  and  $P_x$ -C, respectively, where  $x$  represents the PEDOT:PSS concentration ( $\text{mg mL}^{-1}$ ) in the ink and C indicates the use of CNT dispersion to dissolve the PEDOT:PSS, respectively). e) Photographs of different inks.

printed by DIW at ambient conditions with a high printing speed of  $20 \text{ mm s}^{-1}$  (Figure 2a–d). The printed structures can remain stable after printing due to the modified rheology of the composite ink. The microstructure of the 3D-printed objects after freeze drying was revealed by scanning electron microscopy (SEM) images. Figure 2e shows the surface morphology of a freeze-dried 3D-printed microlattice, from which an overhanging microstructure and a highly open porous surface of the printed filaments are observed. Furthermore, the cross-sectional SEM images clearly show that the CNTs are uniformly and homogeneously dispersed in the cell walls, which could serve as a secondary conducting network to endow the reinforced composite with improved conductive properties (Figure 2f,g). It is worth noting that although the as-printed objects can retain their integrated structures and geometrical features after printing, they are very fragile. This is due to the highly reversible interactions between the components. These reversible interactions are crucial to achieve the shear-thinning behavior of the ink and prevent the printed structure from collapsing after printing. However, they are not strong enough and unable to provide satisfactory mechanical properties (e.g., flexibility and elasticity) for the printed objects. Besides, the as-printed devices still contain electrically insulating PSS and other additives (carboxymethyl cellulose, CMC, from the CNTs dispersion) used to improve the solution processability of PEDOT and CNTs, which significantly hinder the interdomain charge carrier transport, resulting in poor conductivity. Thus, in order to satisfy the requirements of practical functional applications, proper post-printing treatments are required to convert the

printed objects into integrated hydrogels, ensuring satisfactory electrical conductivity and mechanical properties.

In general, the conversion of the printed gel-like PEDOT:PSS-based objects into robust hydrogels relies on a gelation process, and the improvement of conductive properties can be achieved by removing the excess PSS phase while increasing the crystallinity of the PEDOT phase.<sup>[22,24]</sup> However, commonly used post-treatment methods such as acid-assisted hydrothermal and thermal annealing processes,<sup>[4,15]</sup> can efficiently remove the PSS phase and enable enhanced interfacial interactions but would also affect the shape and structure of the resultant PEDOT:PSS materials due to the drastic reaction and rapid compositional change during the treatments. This inevitably leads to low shape fidelity when these methods are directly applied to printed objects. In the present work, a freeze–thawing treatment was employed to enable the precise conversion of the printed PEDOT:PSS-based devices into robust hydrogels, which can facilitate the gelation of the printed devices while preventing their deformation, simultaneously ensuring efficient performance improvement and high printing fidelity (Figure 2h). In a typical process, the printed object was first frozen at  $-20 \text{ }^\circ\text{C}$  after printing. During this step, ice would grow in the object and the solid components can be extruded and densified by the ice crystals to form a skeleton structure. Then, the frozen device was quickly transferred into a low-concentration  $\text{H}_2\text{SO}_4$  solution for thawing, enabling mild gelation and initial solidification of the printed structure. The printed object after the freeze–thawing process exhibited a greatly improved structural robustness

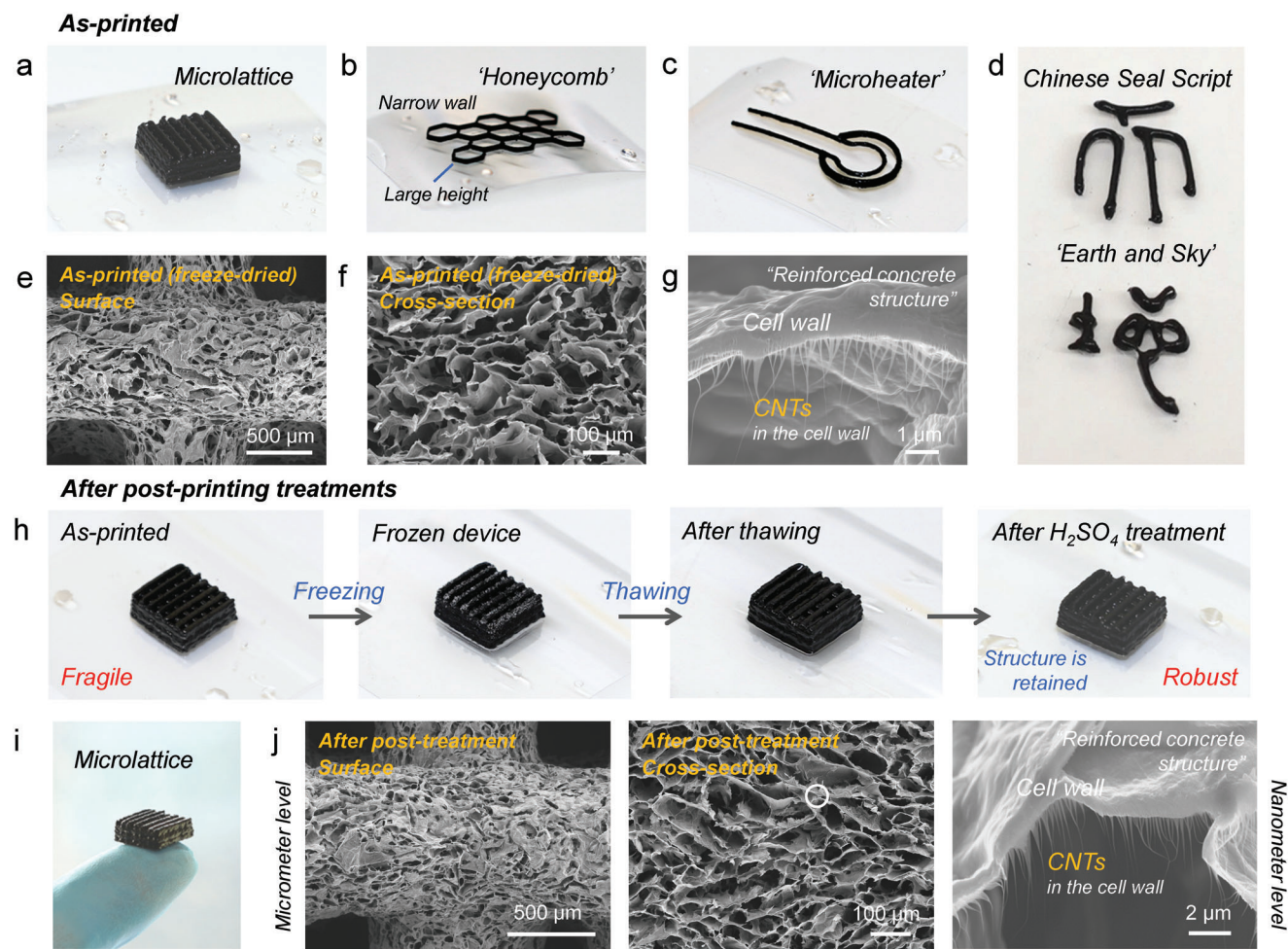


**Figure 2.** 3D printing of composite inks and post-printing treatments. a–d) Photographs of printed architectures. e–g) SEM images of freeze-dried printed microlattice architecture. h) Post-treatment process for converting the printed devices into robust hydrogel devices while enabling high-shape fidelity. i) Printed hydrogel microlattice after the post-printing treatment. j) SEM images of the printed hydrogel, showing that its microstructure is not affected after the post-printing treatment.

and can be easily handled. Finally, the thawed object was treated with high-concentration  $\text{H}_2\text{SO}_4$  to further dissolve the PSS and additives, and to increase the crystallinity of the PEDOT phase, ensuring a strong gelation and an enhancement of the mechanical and electrical properties of the hydrogel. It can be clearly observed that both the gross geometry and structure of the printed hydrogel were not significantly affected during the post-treatments (Figure 2h). The obtained hydrogel is robust and retains the highly open porous structure with the CNTs homogeneously distributed in the cell walls (Figure 2i,j). Therefore, with the assistance of the post-printing freeze–thawing treatment, the printed PEDOT:PSS-based devices can be successfully converted into robust hydrogel devices with high shape fidelity.

To further ascertain the gelation mechanism, X-ray photoelectron spectroscopy (XPS) was employed to reveal the compositional evolution of the samples during the post-treatment. In the high-resolution S 2p spectra, two dominating peaks at 164 and 168 eV can be observed for the as-printed composite samples, which are associated with the PSS and PEDOT phases, respec-

tively (Figure 3a).<sup>[25]</sup> After the post-treatment, the peak intensity ratio of PSS:PEDOT was significantly decreased, indicating that the PSS component was partially removed.<sup>[15]</sup> The successful partial removal of PSS was further confirmed by the C 1s spectra. Figure 3b shows that the  $\text{H}_2\text{SO}_4$ -treated composite hydrogel possesses a much higher areal ratio between the C–O/C–S peak and the C–C/C=C peak than the as-printed composite samples, corresponding to a higher concentration of PEDOT with respect to PSS.<sup>[26,27]</sup> In addition, the  $\text{H}_2\text{SO}_4$  treatment combined with the freeze–thawing strategy can effectively induce the gelation of the CNTs-based dispersions (Figure S3a, Supporting Information). After freezing the CNTs-based dispersion, thawing the frozen object in low-concentration  $\text{H}_2\text{SO}_4$ , and immersing the thawed object in concentrated  $\text{H}_2\text{SO}_4$ , a freestanding 3D CNTs-based architecture can be obtained. The XPS results demonstrated that the intensity ratio of the carbon to oxygen peaks increased from 1.04 to 1.66 after the post-treatment (Figure S3b–d, Supporting Information), which can be attributed to the removal/carbonization of the CMC components by the  $\text{H}_2\text{SO}_4$  treatment. This is also reflected by the morphological change observed in the SEM images



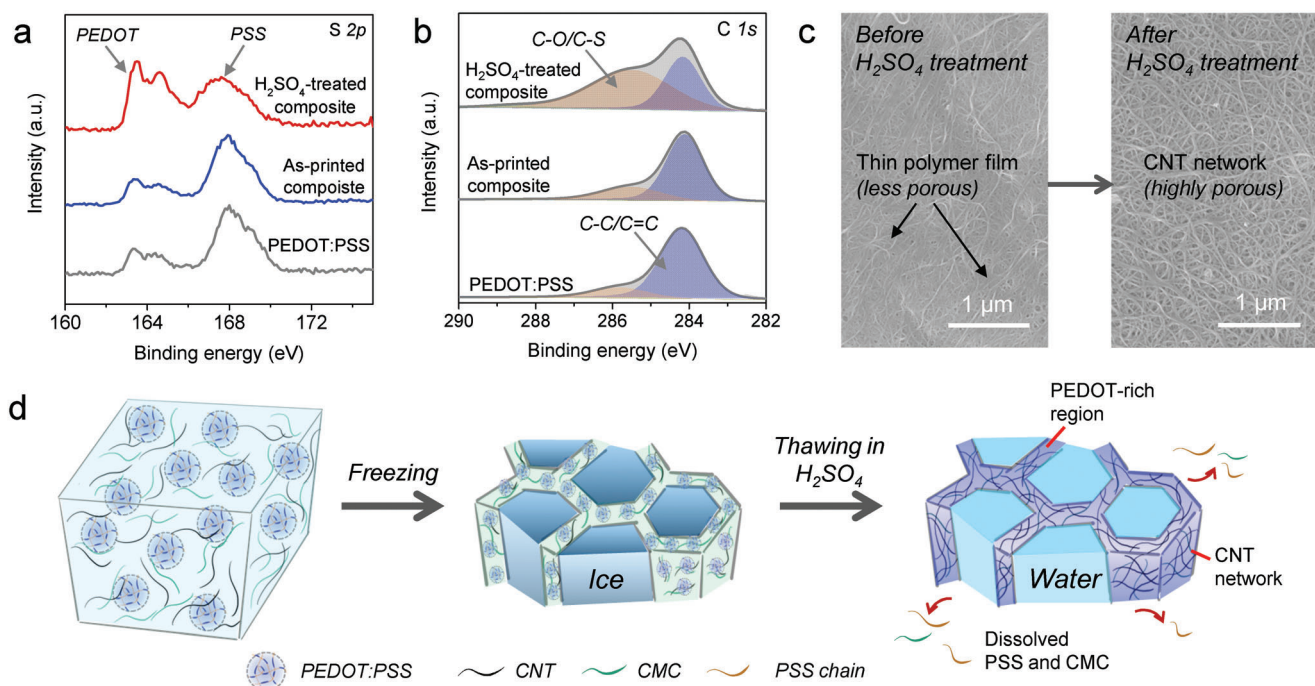


**Figure 3.** Gelation mechanism. a) S 2p and b) C 1s XPS spectra of different samples. c) SEM images showing the morphology of CNTs/CMC film before and after  $H_2SO_4$  treatment. d) Schematic illustrating the gelation process of the printed device during the post-printing process.

and the conductivity variation (Figure 3c and Figure S4, Supporting Information).

Therefore, based on the above analysis, the gelation mechanism of the printed composite hydrogels can be hypothesized, as schematically shown in Figure 3d. First, the freezing process enables the growth of ice crystals in the printed object, and the solid components are extruded and densified at the boundaries between ice crystals, resulting in the formation of a stable skeleton structure. This was verified by the SEM images of the freeze-dried sample shown in Figure 2f. Then, diluted  $H_2SO_4$  slowly diffuses into the frozen structure during the thawing process, mildly and partially removing the PSS components. This has the effect of enhancing interactions between the closely packed components in the skeleton and initially solidifying the printed hydrogel structure. Finally, the concentrated  $H_2SO_4$  treatment further increases the crystallinity of PEDOT and removes the excess insulating polymer components (PSS and CMC), ensuring stronger interfacial interactions between the electrically conductive PEDOT chains and CNTs and enabling the formation of more efficient electron transfer pathways in the resultant hydrogel. Importantly, due to the pre-solidification effect achieved by the freeze–thawing process, volume shrinkage of the printed structure during the high-concentration  $H_2SO_4$  treatment can be effectively prevented. In short, using the proposed ink design and post-printing protocols, highly conductive and robust PEDOT:PSS composite hydrogels can be precisely fabricated by DIW. These hydrogels can perfectly preserve the printed shape and structure after the post-printing treatment, exhibiting high shape fidelity.

In addition to  $H_2SO_4$ , the successful conversion of the printed composite objects into hydrogel devices can also be achieved fol-

lowing the freeze–thawing protocol with the assistance of other solvents, such as HCl, ethylene glycol (EG), and formic acid. Despite their poor PSS extraction ability, these solvents can induce phase separation between PEDOT and PSS and conformational changes of the PEDOT chains,<sup>[24,28,29]</sup> which can strengthen the  $\pi$ -stacking interactions between the conductive PEDOT chains and provide more physical crosslinks,<sup>[15,30]</sup> resulting in successful gelation and enhanced mechanical and conductive properties of the PEDOT:PSS-based hydrogels. In particular, even the nonacidic EG can induce the gelation of the printed PEDOT:PSS-based objects via the freeze–thawing process, resulting in integrated hydrogels. By selecting proper concentrations of the above-mentioned solvents, satisfactory shape fidelity was also achieved after post-treatments (Figure S5, Supporting Information). SEM images showed the porous nature and the homogenous distribution of CNTs in the cell walls of the composite hydrogels treated by different solvents were not affected (Figure S5, Supporting Information), confirming that the post-printing freeze–thawing strategy is a powerful method for realizing the printing applications of PEDOT:PSS-based materials. Although  $H_2SO_4$  treatment has been considered the most effective way for enhancing the conductivity of PEDOT:PSS materials, handling concentrated  $H_2SO_4$  is dangerous and may pose unnecessary risks. Thus, this finding could provide safer alternative manufacturing routes. It is worth noting that the ink design and 3D-printing protocol is also versatile, and other functional additives (e.g., silicon particles) can be easily incorporated into the composite ink to provide additional properties of the printed devices, which would significantly broaden the potential functional applications of the 3D-printed composite materials (Figure S6, Supporting Information).

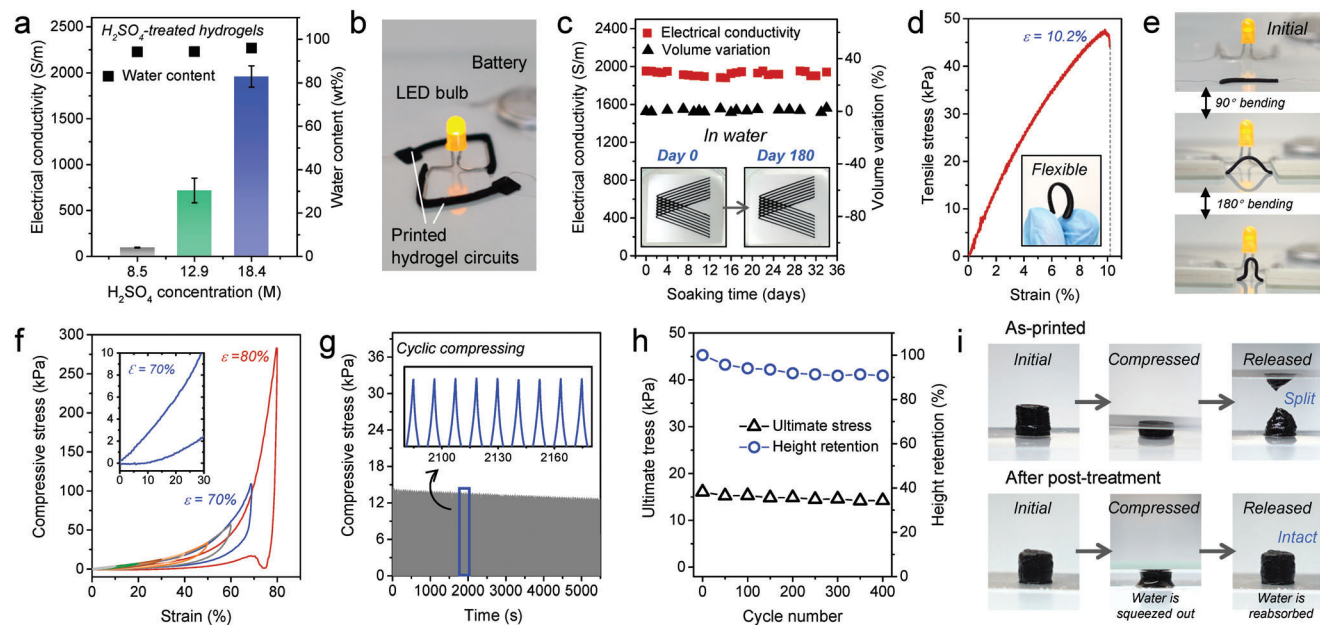


**Figure 4.** a) Electrical conductivities and water contents of hydrogels treated by  $\text{H}_2\text{SO}_4$  with different concentrations. b) Photographs of the hydrogel as a conductor to light up an LED bulb. c) Electrical conductivity and dimension variations of the printed hydrogel sample after immersing in water. d) Tensile stress–strain curve of the printed hydrogel. e) Photographs showing the conductive function of the printed hydrogel under deformation. f) Cyclic compression curves of the printed hydrogel at strains from 10% to 80%. g) The compressive stress curve as a function of time at a cyclic strain of 30%. h) The ultimate stress and relative height of the printed hydrogel for 100 compression cycles. i) Photographs showing the compressibility of the printed hydrogel before and after the post-printing treatment.

Having appropriate conductive and mechanical properties is a prerequisite for the hydrogels to be used for functional applications. After post-printing treatments, the printed hydrogels showed significantly improved electrical conductivity and structural robustness. Previously, PEDOT:PSS/MXene hydrogels with good conductive properties have been fabricated by DIW.<sup>[20]</sup> However, the commercial readiness level of MXene still needs to be further promoted and the spontaneous oxidation of ordinary MXene cannot be completely avoided. In comparison, CNTs, as a carbon material, have unique advantages as functional fillers in PEDOT:PSS due to their abundance, mature synthesis, outstanding electrical properties, and especially excellent stability, which are the key to large-scale production and commercial applications. Through the freeze–thawing and  $\text{H}_2\text{SO}_4$  treatments, the 3D-printed PEDOT:PSS composite hydrogels can exhibit a high electrical conductivity of  $\approx 2000 \text{ S m}^{-1}$  with a water content of 96.0 wt% (Figure 4a). Figure 4b shows the printed hydrogel circuits, which can light up a light-emitting diode (LED) bulb under a low voltage of 3 V, verifying their high conductivity. More importantly, due to the stability of the components and the robustness of the structure, the printed hydrogels also exhibited excellent long-term stability and antiswelling ability in wet environments. After being immersed in water for more than a month, the hydrogels can perfectly keep their shape without observable decrease of their conductivity (Figure 4c). In addition, the printed composite hydrogels are flexible and stretchable with an ultimate tensile strain of 10.2%, and can keep their conducting function unaffected even under large deformations (Figure 4d,e). These results confirmed the reliability of the printed composite hydrogel for long-term practical applications.

Another key requirement for practical applications is that the hydrogels should be elastic, such that the hydrogels can withstand deformations to ensure structural integrity during use and respond to external stimuli. The mechanical properties of the 3D-printed hydrogels were then systematically investigated by performing compression tests. The as-printed samples are very fragile due to the inadequate interfacial interactions existing between the components (Figure 4i). In striking contrast, the composite hydrogels obtained after the post-treatments exhibited outstanding elasticity. Figure 4f shows the compressive stress–strain curves of the printed composite hydrogel at strains of 10%, 20%, 30%, 40%, 50%, 60%, 70%, and 80%, respectively. In the loading process, the hydrogel is densified, squeezing out the water. While in the releasing process, the hydrogel can rapidly recover its original shape even from large strains and reabsorb the surrounding water (Figure 4i). The hydrogels also present satisfactory fatigue resistance and can be repeatedly compressed without observable fracture during the cyclic loading processes (Figure 4g). The height of the hydrogel remained nearly the same as the original value (residual strain  $\approx 9\%$ ) after 400 cyclic compressions at a strain of 30%, while the ultimate stresses only decreased by 4.8% after 100 cycles and 11% after 400 cycles (Figure 4h), indicating the stable elasticity of the hydrogel. The outstanding elasticity can be attributed to the interconnected porous structure and the synergistic effect between the PEDOT:PSS and CNTs. With the formation of a unique binary-network structure (Figure 2j), the CNTs networks that are uniformly embedded in the PEDOT:PSS cell walls could effectively reinforce the hydrogel and enable efficient load transfer upon deformations, resulting in high elasticity.<sup>[31–33]</sup>

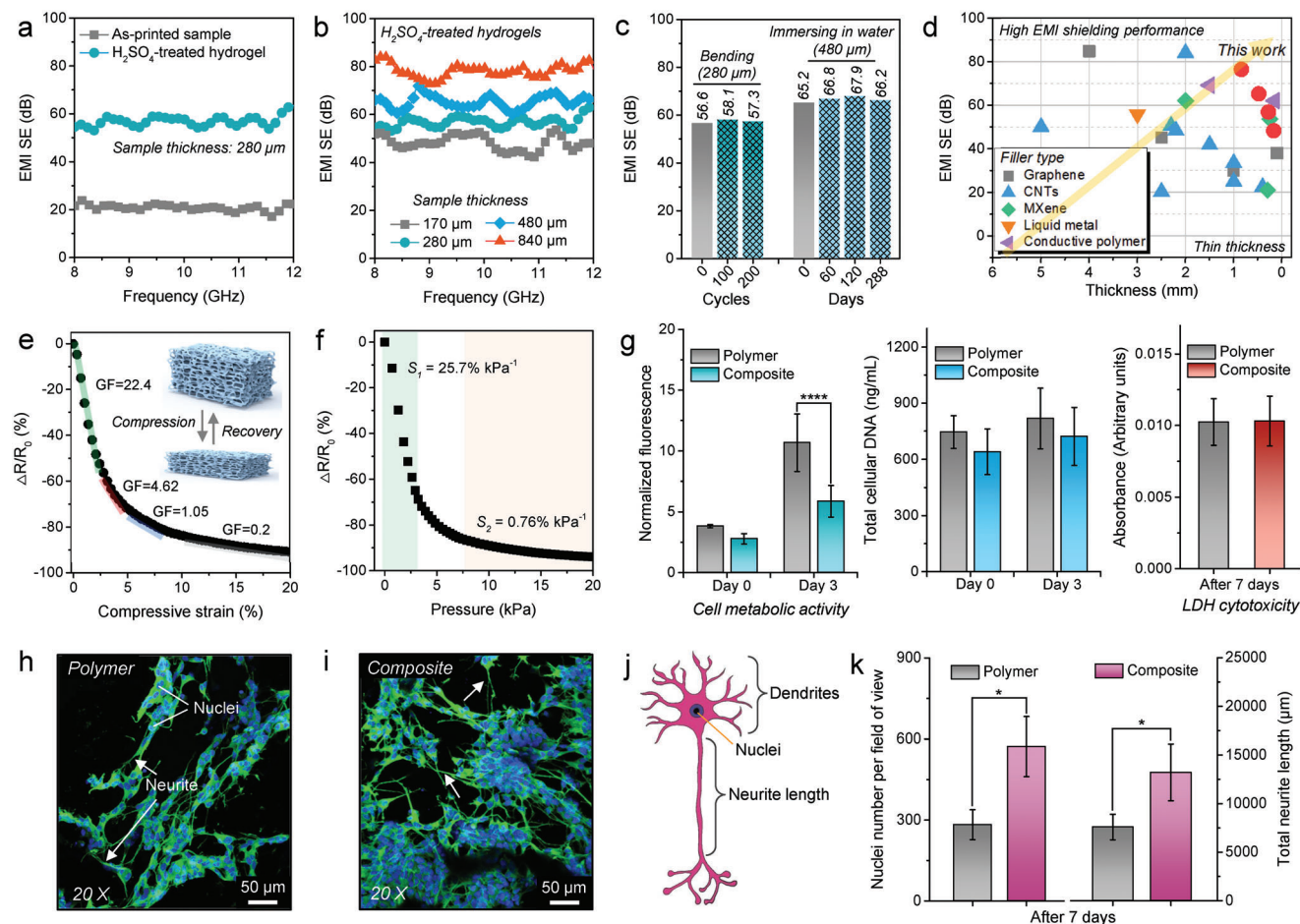


**Figure 5.** EMI shielding, sensing, and biocompatible properties. a) EMI SE of as-printed sample and corresponding hydrogel after post-treatment. b) EMI SE of  $H_2SO_4$ -treated hydrogels with different thicknesses. c) EMI SE of hydrogels after repeated  $90^\circ$  bending deformation and immersing in water for a long time. d) Comparison of the EMI shielding performance of the hydrogel with other polymer-based composites. The changes of electrical resistance as functions of e) compressive strain (inset: schematic illustrating the sensing mechanism) and f) pressure of the hydrogel. g) Metabolic activity (left), total cellular DNA (middle) and LDH cytotoxicity assay (right) of neurons grown directly on different hydrogels. Fluorescence microscopy images of stained neurons grown on h) PEDOT:PSS (polymer) and i) PEDOT:PSS/CNT (composite) samples. j) Schematic illustrating the neuron structure. k) Count of nuclei visible and total length of neurites extended by cells on different samples after 7 days.

With the fast development of wireless communication and high-power electronics, high-performance EMI shielding materials are urgently needed for controlling the electromagnetic radiation interference that seriously affects the normal operation of sensitive electronic apparatus and systems.<sup>[34–37]</sup> Although the conductivity of the printed composite hydrogel is lower than that of some representative EMI shielding materials (e.g., MXene film, graphene film, and metal foil), its conductive nature and high water content can still provide strong conductive and polarization losses to attenuate the incident electromagnetic waves, ensuring outstanding EMI shielding performance.<sup>[38–41]</sup> A 280  $\mu\text{m}$  thick composite hydrogel exhibits an EMI SE of 56.8 dB with a strong absorption behavior (Figure 5a and Figure S7, Supporting Information), which satisfies the requirements of most commercial applications ( $>20$  dB).<sup>[42]</sup> Increasing the hydrogel thickness enables the efficient enhancement of the EMI shielding performance. A superior EMI SE of 76.4 dB can be achieved when the thickness of the hydrogel is 840  $\mu\text{m}$  (Figure 5b). Moreover, due to their good structural robustness and superb sta-

bility, the hydrogels present stable EMI shielding performances even after repeated bending cycles or immersing in water for a long time, highlighting their reliability for practical applications (Figure 5c). Note that a slight deviation in the EMI SE values of the sample was observed, which should be due to the analyzer limitations and sample installation. Since the deviation is less than 5%, the EMI SE was considered not to have changed significantly. As shown in Figure 5d and Table S1 in the Supporting Information, our PEDOT:PSS/CNTs composite hydrogels exhibit both high EMI SE and thin thickness, and are comparable to other state-of-art polymer-based EMI shielding materials. Although excellent EMI shielding performances of polymer composites have been achieved in previous work,<sup>[43–47]</sup> their fabrication still mainly relies on traditional manufacturing strategies, such as casting and molding, which would inevitably limit their applications in situations where fast prototyping or complex design of the shields are needed. Besides, the traditional subtractive manufacturing processes can easily cause damage to soft materials, especially when fabricating miniaturized devices. Thus, the



3D printing of EMI shields that goes beyond the usual manufacturing protocols has great potential to meet the ever-escalating design demands of modern devices.<sup>[42]</sup> Compared with conventional EMI shielding solutions, our high-performance composite hydrogels that are compatible with the 3D-printing technique present unique advantages. This means that customized EMI shielding solutions could be created to precisely fit the users' real needs, and to widen their applications for next-generation applications.

In addition to providing efficient EMI shielding functions, the printed composite hydrogels can be utilized as piezoresistive pressure sensors because of their combination of conductive nature, elasticity, and porous structure (Figure 5e, inset).<sup>[48]</sup> When external pressure is applied to the hydrogel, the deformation of its porous structure results in an increased contact area of the cell wall, leading to electrical resistance changes.<sup>[49]</sup> Meanwhile, when the pressure is released, the porous structure can spring back to its original state due to the elasticity, enabling the recovery of the resistance. As a result, the hydrogel can stably and repeatedly respond to external pressure stimuli. Figure 5f presents plots of resistance change against compressive strain of the printed composite hydrogel, and the gauge factor can be determined as 22.4 within the strain range of 0–3%. The compressive force-induced deformation of the porous structure enables the hydrogel to exhibit a pressure sensitivity of 25.7% kPa<sup>-1</sup>, and the hydrogel can stably respond to cyclic compressing–releasing with different pressures (Figure 5f and Figure S8, Supporting Information). The sensitivity then decreased to 0.76% kPa<sup>-1</sup> under higher pressures because the conductive pathway would approach saturation upon continuous pressing. It is worth noting that the HCl-treated hydrogels with inferior electrical conductivity have a lower EMI SE (42.4 dB at a thickness of 290 μm) but a much higher pressure sensitivity of 85.5% kPa<sup>-1</sup> (Figure S9, Supporting Information). This is because the conducting network of the HCl-treated hydrogels with lower conductivity is supposed to be easier to change its structure upon compression than the H<sub>2</sub>SO<sub>4</sub>-treated hydrogels, resulting in higher pressure sensitivity.<sup>[50,51]</sup> These composite hydrogels are soft and have similar moduli to human tissues, thus holding great potential for wearable and implantable applications.

Considering the potential applications of printed composite hydrogels as implantable devices and bioelectronics, we also investigated their biocompatibility by directly growing neurons on the hydrogels and assessing their morphology, cell metabolic rate, total cellular DNA, and cytotoxicity in vitro. The printed pure PEDOT:PSS hydrogels were used as a control because PEDOT:PSS materials have been previously proved to be biocompatible.<sup>[52,53]</sup> Cell metabolic activity results indicated no significant difference between groups after 24 h. The metabolic rate increased in both groups, but the metabolic rate of cells on pure PEDOT:PSS was significantly higher than that of cells on composite hydrogel (Figure 5g, left), suggesting that cells are less stressed on the composite samples. Total cellular DNA remained almost consistent across groups at different time points, indicating that the population of the adherent cells was well maintained on both PEDOT:PSS and composite hydrogels (Figure 5g, middle). Lactate dehydrogenase (LDH) cytotoxicity testing further showed no difference in levels between the two groups after 7 days (Figure 5g, right). Therefore, the obtained composite hydro-

gel well maintained good biocompatibility despite the addition of CNTs to improve ink rheology and hydrogel performance. In addition, confocal microscopy images showed both the polymer and composite hydrogels can support the survival and growth of neurons (Figure 5h,i). The cells grown on the hydrogels exhibited healthy neuronal morphologies, with long neurites observed extending between cells (Figure 5j), indicating that the hydrogels can provide a neurotrophic environment that encouraged the neurite outgrowth. Interestingly, although both hydrogels can support cell growth, the cell viability and proliferation were better on the composite hydrogel, as verified by the number of nuclei and the fractional area stained with β-III tubulin (Figure 5k and Figure S10, Supporting Information). Moreover, the total neurite length was significantly increased on the composite hydrogels with a value of 13215.3 ± 2916.7 μm, which is significantly higher than 7588.7 ± 1319.4 μm on the PEDOT:PSS hydrogels, suggesting that the composite hydrogel can effectively promote neuron and neurite growth. This effect on neuronal growth and development is likely due to the interaction of the neurons with the CNTs embedded in the composite, which has been observed to promote markers of neuronal development in other studies.<sup>[54–56]</sup> Therefore, with the combination of the promising properties, customizability, and excellent biocompatibility, the 3D-printed composite hydrogels also hold great potential for implantable and tissue engineering applications.

### 3. Conclusion

In summary, we presented a simple and effective ink preparation and 3D-printing method for the customizable and reproducible fabrication of multifunctional conductive polymer composite hydrogels based on fully commercially available raw materials. The facile ink preparation and solid printing processes also allow that functional additives can be easily incorporated into the hydrogels to broaden their potential applications. The printed composite hydrogels exhibited high water content, good electrical conductivity, outstanding elasticity, and favorable biocompatibility, and can provide efficient EMI shielding and pressure-sensing functions. We believe this work will bring new opportunities to functional conductive hydrogels and facilitate their development from the laboratory to commercial applications in wearable and implantable devices, soft robotics, and bioelectronics.

### 4. Experimental Section

**Preparation of 3D Printable Composite Ink:** All reagents were used as received without further purification. The PEDOT:PSS was obtained by freeze-drying the commercially available PEDOT:PSS solution (Clevios PH1000, Heraeus Electronic Materials). The CNT aqueous dispersion (0.2 wt% CNT in water, ≈0.3 wt% CMC as a surfactant stabilizer) was supplied by Tuball, OCSiAl. The freeze-dried PEDOT:PSS was then mixed with the CNTs dispersion in a mortar by grinding. Finally, the resulting paste-like ink was collected and stored in a fridge at 4 °C before use. The pure PEDOT:PSS ink was obtained by adding the freeze-dried PEDOT:PSS into deionized water followed by vortex mixing. The silicon-containing ink was obtained by adding the silicon particles and the freeze-dried PEDOT:PSS to the CNTs dispersion, followed by grinding in a mortar. The details of different inks with various PEDOT:PSS mass ratios are presented in Table S2, Supporting Information.

**3D Printing and Post-Printing Treatments:** The 3D-printing process was conducted on a benchtop 3D printer (nano3Dprint). The patterns were

designed and converted into G-code by commercial software, Shapr 3D and Simplify3D, respectively. After printing, the printed objects were first frozen at  $-20^{\circ}\text{C}$ . Then the frozen objects were transferred into 5 M  $\text{H}_2\text{SO}_4$  or HCl at room temperature to initiate a mild gelation. After thawing, the freestanding gel-like objects were immersed into high-concentration  $\text{H}_2\text{SO}_4$  (18.4 M) or HCl (12 M) at room temperature for 24 h. Finally, the as-obtained hydrogel objects were washed and dialyzed in deionized water to remove the acid. All the resulting hydrogels were stored in water at room temperature.

**Characterization:** The rheological behaviors of the composite inks were tested on a Discovery HR-2 Rheometer (TA Instruments) with a steel parallel-plate geometry (8 mm diameter) at  $20^{\circ}\text{C}$ . All samples were allowed to rest for 30 min prior to testing. Morphologies and microstructure of the samples were observed by a Zeiss Ultra Plus SEM (Carl Zeiss, Germany). The electrical resistance was measured by a two-point probe method (Keithley 2400) and the electrical conductivity was calculated using the equation  $\sigma = L/(RA)$ , where  $R$ ,  $L$ , and  $A$  are the electrical resistance, the length, and the conductive path area of a hydrogel, respectively. The solid content was obtained by calculating the weight ratio of the as-obtained hydrogel and the corresponding freeze-dried aerogel. In order to measure the volume variation of the composite hydrogel, a cuboid sample was printed. And the volume variation (%) was determined by  $(V_x - V_0) \times 100\%/V_0$ , where  $V_0$  is the volume of the as-obtained hydrogel and  $V_x$  is the volume of the hydrogel after being immersed in water for  $x$  days. Tensile and compressive properties were studied with a Zwick Z0.5 Proline Tensile Tester. The electromechanical properties of the pressure sensor were tested using a Keithley KE2601 source meter controlled by LabView software in conjunction with the universal tester. EMI shielding performances were measured by a Rohde & Schwarz ZVB 20 vector network analyzer with a waveguide method in the frequency range within 8–12 GHz.

**Biocompatibility of Hydrogels:** SH-SY5Y human neuronal cell line cells (CRL-2266, ATCC) were seeded and grown directly on printed hydrogels. Briefly, the cells were first grown and seeded in a medium consisting of Dulbecco's modified Eagle medium/nutrient mixture F-12 (Sigma-Aldrich) with 10% fetal bovine serum (Biosera), 1% penicillin/streptomycin (Sciencell), and 1% L-glutamine (Sigma-Aldrich). Cell metabolic rate and total cellular DNA were assessed using an Alamar Blue assay kit (Invitrogen) and a Pico Green dsDNA assay kit (Invitrogen), respectively. Cytotoxicity was assessed using a CyQuant LDH assay kit (Invitrogen). For neurite outgrowth experiments, the growth medium was exchanged to differentiation media after 24 h, consisting of Neurobasal Medium (Gibco) with 1% penicillin/streptomycin, 1% Glutamax (Gibco), 2% B27 (Gibco), and 0.003% ATRA (Sigma-Aldrich). The neurons were then allowed to grow for 6 days in this medium. Thereafter, samples were immersed in 10% formalin for 30 min at room temperature and washed with phosphate buffered saline (PBS). Neurons were immunostained with anti-rabbit  $\beta$  Tubulin III Antibody (1:1000, T2200, Sigma-Aldrich) in 0.1 M PBS with 0.2% Triton-X100 (PBT) at  $4^{\circ}\text{C}$  overnight. Samples were then washed with PBS (x3) and secondary immunostained with a Goat Anti-Rabbit 555 secondary antibody (1:1000, A32732, Invitrogen). Following this, samples were washed with PBS (x3), and neuronal nuclei were stained with 4',6-diamidino-2-phenylindole (Thermo Fisher Scientific). The samples were imaged using a Zeiss 710 NLO confocal microscope to assess neurite outgrowth. Outgrowth was assessed using ImageJ software and an established Neurite-Tracer plugin for automated neurite outgrowth analysis. Cell nuclei were counted and total neurite length per image was measured and used to calculate average neurite length per cell. This was averaged across four images per sample to return an average value for each sample.

**Statistical Analysis:** For biological characterizations, all results represented at least three repeated individual experiments ( $N > 3$ ) with at least three technical replicates per experiment ( $n > 3$ ). Data sets were tested for normality using the appropriate tests (Shapiro–Wilk, Kolmogorov–Smirnov) and statistically assessed using parametric ( $t$ -test, one-way analysis of variance) or nonparametric (Mann–Whitney) tests where appropriate. Statistical analysis was carried out using GraphPad Prism (v8.0.1) software and all values were represented as the mean and error bars as the standard error of the mean (SEM).

## Supporting Information

Supporting Information is available from the Wiley Online Library or from the author.

## Acknowledgements

The authors thank the Advanced Microscopy Laboratory for the provision of their facilities. This publication has emanated from research supported in part by a research grant from Science Foundation Ireland (SFI) AMBER (12/RC/2278\_P2), co-funded under the European Research Council (ERC) CoG 3D2Dprint (GA 681544) and PoC 2D\_EMI Shielding (GA 101059920). F.J.O'B., A.D., and L.L. acknowledge the financial support of a joint funding initiative between the Irish Rugby Football Union Charitable Trust (IRFU-CT) and the SFI AMBER (SFI/12/RC/2278).

Open access funding provided by IReL.

## Conflict of Interest

The authors declare no conflict of interest.

## Data Availability Statement

Research data are not shared.

## Keywords

3D printing, electromagnetic interference shielding, hydrogels, multifunctionality, PEDOT:PSS

Received: December 5, 2022

Revised: May 4, 2023

Published online: May 23, 2023

- [1] Y. Zhao, C.-Y. Lo, L. Ruan, C.-H. Pi, C. Kim, Y. Alsaïd, I. Frenkel, R. Rico, T.-C. Tsao, X. He, *Sci. Rob.* **2021**, 6, eabd5483.
- [2] Y. Liu, J. Liu, S. Chen, T. Lei, Y. Kim, S. Niu, H. Wang, X. Wang, A. M. Foudeh, J. B. H. Tok, Z. Bao, *Nat. Biomed. Eng.* **2019**, 3, 58.
- [3] T. Li, G. Li, Y. Liang, T. Cheng, J. Dai, X. Yang, B. Liu, Z. Zeng, Z. Huang, Y. Luo, T. Xie, W. Yang, *Sci. Adv.* **2017**, 3, e1602045.
- [4] B. Lu, H. Yuk, S. Lin, N. Jian, K. Qu, J. Xu, X. Zhao, *Nat. Commun.* **2019**, 10, 1043.
- [5] B. W. Walker, R. Portillo Lara, E. Mogadam, C. Hsiang Yu, W. Kimball, N. Annabi, *Prog. Polym. Sci.* **2019**, 92, 135.
- [6] J. Li, C. Wu, P. K. Chu, M. Gelinsky, *Mater. Sci. Eng., R* **2020**, 140, 100543.
- [7] R. L. Truby, J. A. Lewis, *Nature* **2016**, 540, 371.
- [8] Q. Ge, Z. Chen, J. Cheng, B. Zhang, Y.-F. Zhang, H. Li, X. He, C. Yuan, J. Liu, S. Magdassi, S. Qu, *Sci. Adv.* **2021**, 7, eaba4261.
- [9] Z. Wang, H. Cui, M. Liu, S. L. Grage, M. Hoffmann, E. Sedghamiz, W. Wenzel, P. A. Levkin, *Adv. Mater.* **2022**, 34, 2107791.
- [10] M.-J. Yin, M. Yao, S. Gao, A. P. Zhang, H.-Y. Tam, P.-K. A. Wai, *Adv. Mater.* **2016**, 28, 1394.
- [11] F. Gao, Z. Xu, Q. Liang, B. Liu, H. Li, Y. Wu, Y. Zhang, Z. Lin, M. Wu, C. Ruan, W. Liu, *Adv. Funct. Mater.* **2018**, 28, 1706644.
- [12] C. Wang, S. S. Rubakhin, M. J. Enright, J. V. Sweedler, R. G. Nuzzo, *Adv. Funct. Mater.* **2021**, 31, 2010246.
- [13] H. Yuk, B. Lu, S. Lin, K. Qu, J. Xu, J. Luo, X. Zhao, *Nat. Commun.* **2020**, 11, 1604.

- [14] Z. Chen, D. Zhao, B. Liu, G. Nian, X. Li, J. Yin, S. Qu, W. Yang, *Adv. Funct. Mater.* **2019**, *29*, 1900971.
- [15] B. Yao, H. Wang, Q. Zhou, M. Wu, M. Zhang, C. Li, G. Shi, *Adv. Mater.* **2017**, *29*, 1700974.
- [16] M. Moussa, M. F. El-Kady, D. Dubal, T. T. Tung, M. J. Nine, N. Mohamed, R. B. Kaner, D. Losic, *ACS Appl. Energy Mater.* **2020**, *3*, 923.
- [17] S. Zhang, Y. Chen, H. Liu, Z. Wang, H. Ling, C. Wang, J. Ni, B. Çelebi-Saltik, X. Wang, X. Meng, H.-J. Kim, A. Baidya, S. Ahadian, N. Ashammakhi, M. R. Dokmeci, J. Travas-Sejdic, A. Khademhosseini, *Adv. Mater.* **2020**, *32*, 1904752.
- [18] F. Fu, J. Wang, H. Zeng, J. Yu, *ACS Mater. Lett.* **2020**, *2*, 1287.
- [19] C. Zhang, M. Wang, C. Jiang, P. Zhu, B. Sun, Q. Gao, C. Gao, R. Liu, *Nano Energy* **2022**, *95*, 106991.
- [20] J. Liu, L. Mckee, J. Garcia, S. Pinilla, S. Barwich, M. Möbius, P. Stamenov, J. N. Coleman, V. Nicolosi, *Adv. Mater.* **2022**, *34*, 2106253.
- [21] J. Wang, Q. Li, K. Li, X. Sun, Y. Wang, T. Zhuang, J. Yan, H. Wang, *Adv. Mater.* **2022**, *34*, 2109904.
- [22] N. Kim, S. Kee, S. H. Lee, B. H. Lee, Y. H. Kahng, Y.-R. Jo, B.-J. Kim, K. Lee, *Adv. Mater.* **2014**, *26*, 2268.
- [23] J. Qian, Q. Chen, M. Hong, W. Xie, S. Jing, Y. Bao, G. Chen, Z. Pang, L. Hu, T. Li, *Mater. Today* **2022**, *54*, 18.
- [24] Y. Xia, J. Ouyang, *ACS Appl. Mater. Interfaces* **2010**, *2*, 474.
- [25] Y. Xia, K. Sun, J. Ouyang, *Adv. Mater.* **2012**, *24*, 2436.
- [26] H. Park, S. H. Lee, F. S. Kim, H. H. Choi, I. W. Cheong, J. H. Kim, *J. Mater. Chem. A* **2014**, *2*, 6532.
- [27] R. Sarabia-Riquelme, R. Andrews, J. E. Anthony, M. C. Weisenberger, *J. Mater. Chem. C* **2020**, *8*, 11618.
- [28] Y. H. Kim, C. Sachse, M. L. Machala, C. May, L. Müller-Meskamp, K. Leo, *Adv. Funct. Mater.* **2011**, *21*, 1076.
- [29] D. A. Mengistie, M. A. Ibrahim, P.-C. Wang, C.-W. Chu, *ACS Appl. Mater. Interfaces* **2014**, *6*, 2292.
- [30] H. C. Lim, S. H. Min, E. Lee, J. Jang, S. H. Kim, J.-I. Hong, *ACS Appl. Mater. Interfaces* **2015**, *7*, 11069.
- [31] Y. Qin, Q. Peng, Y. Ding, Z. Lin, C. Wang, Y. Li, F. Xu, J. Li, Y. Yuan, X. He, Y. Li, *ACS Nano* **2015**, *9*, 8933.
- [32] M. Yang, N. Zhao, Y. Cui, W. Gao, Q. Zhao, C. Gao, H. Bai, T. Xie, *ACS Nano* **2017**, *11*, 6817.
- [33] J. N. Coleman, M. Cadec, R. Blake, V. Nicolosi, K. P. Ryan, C. Belton, A. Fonseca, J. B. Nagy, Y. K. Gun'ko, W. J. Blau, *Adv. Funct. Mater.* **2004**, *14*, 791.
- [34] Q. Wei, S. Pei, X. Qian, H. Liu, Z. Liu, W. Zhang, T. Zhou, Z. Zhang, X. Zhang, H.-M. Cheng, W. Ren, *Adv. Mater.* **2020**, *32*, 1907411.
- [35] J. Liu, H.-B. Zhang, R. Sun, Y. Liu, Z. Liu, A. Zhou, Z.-Z. Yu, *Adv. Mater.* **2017**, *29*, 1702367.
- [36] A. Iqbal, F. Shahzad, K. Hantanasirisakul, M.-K. Kim, J. Kwon, J. Hong, H. Kim, D. Kim, Y. Gogotsi, C. M. Koo, *Science* **2020**, *369*, 446.
- [37] Z. Zeng, F. Jiang, Y. Yue, D. Han, L. Lin, S. Zhao, Y.-B. Zhao, Z. Pan, C. Li, G. Nyström, J. Wang, *Adv. Mater.* **2020**, *32*, 1908496.
- [38] Y. Zhu, J. Liu, T. Guo, J. J. Wang, X. Tang, V. Nicolosi, *ACS Nano* **2021**, *15*, 1465.
- [39] Y. Yu, P. Yi, W. Xu, X. Sun, G. Deng, X. Liu, J. Shui, R. Yu, *Nano-Micro Lett.* **2022**, *14*, 77.
- [40] Y. Yang, N. Wu, B. Li, W. Liu, F. Pan, Z. Zeng, J. Liu, *ACS Nano* **2022**, *16*, 15042.
- [41] Z. Zhao, L. Zhang, H. Wu, *Adv. Mater.* **2022**, *34*, 2205376.
- [42] T. Yun, H. Kim, A. Iqbal, Y. S. Cho, G. S. Lee, M.-K. Kim, S. J. Kim, D. Kim, Y. Gogotsi, S. O. Kim, C. M. Koo, *Adv. Mater.* **2020**, *32*, 1906769.
- [43] D.-X. Yan, H. Pang, B. Li, R. Vajtai, L. Xu, P.-G. Ren, J.-H. Wang, Z.-M. Li, *Adv. Funct. Mater.* **2015**, *25*, 559.
- [44] X. Jia, B. Shen, L. Zhang, W. Zheng, *Carbon* **2021**, *173*, 932.
- [45] Z. Chen, C. Xu, C. Ma, W. Ren, H.-M. Cheng, *Adv. Mater.* **2013**, *25*, 1296.
- [46] R. Sun, H.-B. Zhang, J. Liu, X. Xie, R. Yang, Y. Li, S. Hong, Z.-Z. Yu, *Adv. Funct. Mater.* **2017**, *27*, 1702807.
- [47] H. Abbasi, M. Antunes, J. I. Velasco, *Prog. Mater. Sci.* **2019**, *103*, 319.
- [48] P. Min, X. Li, P. Liu, J. Liu, X.-Q. Jia, X.-P. Li, Z.-Z. Yu, *Adv. Funct. Mater.* **2021**, *31*, 2103703.
- [49] Y. Ma, Y. Yue, H. Zhang, F. Cheng, W. Zhao, J. Rao, S. Luo, J. Wang, X. Jiang, Z. Liu, N. Liu, Y. Gao, *ACS Nano* **2018**, *12*, 3209.
- [50] H. Chen, Z. Su, Y. Song, X. Cheng, X. Chen, B. Meng, Z. Song, D. Chen, H. Zhang, *Adv. Funct. Mater.* **2017**, *27*, 1604434.
- [51] J. Yang, Y. Ye, X. Li, X. Lü, R. Chen, *Compos. Sci. Technol.* **2018**, *164*, 187.
- [52] T. Teshima, H. Nakashima, N. Kasai, S. Sasaki, A. Tanaka, S. Tsukada, K. Sumitomo, *Adv. Funct. Mater.* **2016**, *26*, 8185.
- [53] A. Zhuang, X. Huang, S. Fan, X. Yao, B. Zhu, Y. Zhang, *ACS Appl. Mater. Interfaces* **2022**, *14*, 123.
- [54] G.-Z. Jin, M. Kim, U. S. Shin, H.-W. Kim, *Neurosci. Lett.* **2011**, *501*, 10.
- [55] G. Cellot, E. Cilia, S. Cipollone, V. Rancic, A. Sucapane, S. Giordani, L. Gambazzi, H. Markram, M. Grandolfo, D. Scaini, F. Gelain, L. Casalis, M. Prato, M. Giugliano, L. Ballerini, *Nat. Nanotechnol.* **2009**, *4*, 126.
- [56] A. Fabbro, A. Villari, J. Laishram, D. Scaini, F. M. Toma, A. Turco, M. Prato, L. Ballerini, *ACS Nano* **2012**, *6*, 2041.